Optimization and Scheduling of Heat Pump Energy Storage Coupling System Considering Carbon Certification Synergy and Response Characteristics

Shenbo Yang[1], Yan Liang[2, 3], Shaokang Qi[4], Yuanying Chi[1], Ming Zhou[2], Junyao Shen[4]*

[1]College of Economics and Management, Beijing University of Technology, Chaoyang Beijing, 100124, China
[2]School of Electrical and Electronic Engineering, North China Electric Power University,
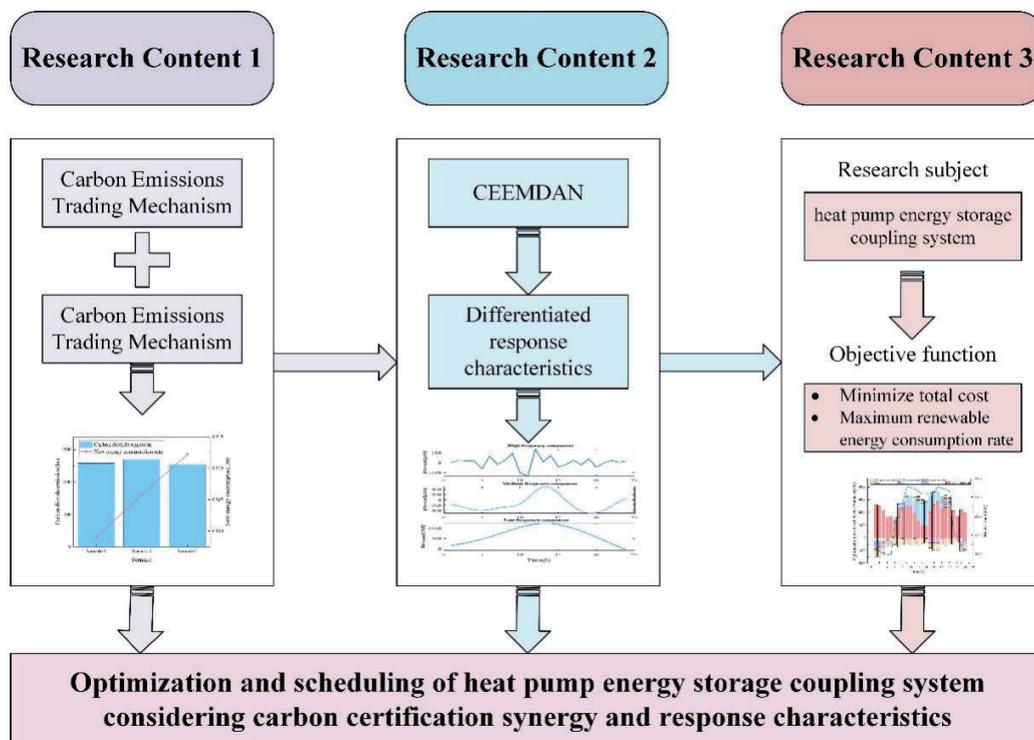Changping Beijing, 102206, China
[3]Economic and Technical Research Institute of Shanxi Electrical Power Company of SGCC, Taiyuan, 030000, China
[4]School of Economics and Management, North China Electric Power University, Changping Beijing, 102206, China

Abstract

*e-mail: shenjunyao24@163.com

In order to solve the problems of low energy cascade utilization degree, insufficient analysis of response characteristics of equipment differentiation, and prominent low-carbon demand in the integrated energy system, this paper researches the optimization scheduling of heat pump energy storage coupling systems considering carbon certification synergy and response characteristics. Firstly, a system operation framework and mathematical model were constructed using the heat pump energy storage coupling system as the research object. Secondly, a carbon certification collaborative mechanism was designed, and the uncertainties in the coupled system were decomposed based on the CEEMDAN-IIR method to match the response characteristics of the equipment. Thirdly, a coupled system operation optimization model was constructed to minimize the total system cost and maximize new energy consumption. Finally, an empirical analysis was conducted to verify the model's effectiveness using a certain coupled system as an example. The results of the example show that: 1) The heat pump energy storage coupling system can reduce operating costs by 22.5% compared to other systems; 2) Compared with the carbon certificate collaborative mechanism, a single carbon trading mechanism increases carbon dioxide emissions by 20.48 kg and reduces the new energy consumption rate by 1.32%; 3) Compared with the EMD algorithm and EEMD algorithm, the CEEMDAN-IIR method can more effectively suppress false modes, and improve the stability and accuracy of decomposition.

Introduction

The integrated energy system involves different types of energy, such as electricity and heat. Due to the complex system form, multiple types of equipment, and significant differences in the characteristics of different energy systems, it is technically difficult to couple and ensure the coordinated matching of various energy systems. The integrated energy system has problems such as low energy cascade utilization, insufficient analysis of equipment's differentiation response characteristics, and prominent low-carbon demand [1-2]. To address these issues, firstly, it is urgent to utilize the complementary characteristics of complex storage and easy transportation of electrical energy and easy storage of heat, coupling heat pumps with thermal storage devices to achieve the mutual conversion of electricity and heat, effectively improving the energy utilization efficiency of the integrated energy system [3]. Secondly, it is urgent to analyze the differentiated characteristics of the equipment and improve the system's flexible scheduling capability [4]. Thirdly, with the development of carbon emission trading (CET) and green certificate trading (GCT), it is urgent to explore the development mechanism of the integrated energy system in these two markets and promote the low-carbon development of the system. On this basis, how to coordinate these three issues to achieve optimal operation of the coupled system has become a key issue.

Regarding the research on integrated energy systems, scholars have conducted related studies on electric thermal integrated energy systems. Smith et al. [5] proposed a dynamic energy flow calculation model for electric thermal integrated energy systems through the unified energy path theory and analyzed the feasibility of electric thermal complementarity. Aragao et al. [6]

proposed a multi-time scale dynamic optimization (MSDO) method for ultra-short-term scheduling of industrial electric thermal gas integrated energy systems by analyzing the optimal minimum time granularity, which utilizes the thermal energy of industrial parks. Li et al. [7] utilized waste heat in data centers by constructing an electric thermal integrated energy system. Nord et al. [8] constructed an integrated energy system design optimization model that considers the economic level of farmers and zero carbon constraints, utilizing the thermal energy of buildings. Based on the short-term utilization of thermal energy, Hugo et al. [9] discussed the role of seasonal thermal energy storage in promoting renewable energy consumption and reducing CO_2 emissions. Novo et al. [10] constructed a regional integrated energy system that includes seasonal thermal storage and ground source heat pumps, fully utilizing geothermal energy and reducing operating costs by 9%.

Scholars have conducted separate studies on CET and GCT mechanisms. In terms of research on CET, Xu et al. [11] introduced the tiered CET into integrated energy systems and verified through numerical examples that the tiered carbon trading mechanism can significantly reduce carbon emissions. Based on the literature [11], Li et al. [12] proposed a stepped carbon tax method to efficiently control carbon emissions. Huo et al. [13] constructed a seasonal CET based on the carbon emission characteristics of the system at different time periods. In the research on the GCT mechanism, Wang et al. [14-15] used fixed carbon emission factors to conduct carbon emission accounting, established an integrated energy system optimization model considering GCT costs, imposed economic penalties on excess carbon emissions, and promoted the reduction of carbon emissions in the integrated energy system. Based on single CET and GCT, Wang et al. [16]

considered the coupling of GCT and CET mechanisms under the diversified utilization of hydrogen energy and constructed a multi-time scale optimization model for the integrated energy system of diversified utilization of hydrogen energy.

Regarding the uncertainty of integrated energy systems, existing research mostly achieves load peak shaving and valley filling through demand response or uses energy storage technology to smooth the fluctuations of uncertain variables [17-18]. On this basis, some scholars reduce system uncertainty by analyzing the characteristics of the equipment. Jin et al. [19-20] constructed dynamic models of the variable operating conditions of equipment such as gas turbines, gas boilers, and absorption refrigerants to reduce the uncertainty of system operation.

The existing research focuses on constructing operation optimization models for electric thermal integrated energy systems, but there are three shortcomings: 1) Existing research has utilized thermal energy on both short-term and long-term scales while verifying the feasibility of electric thermal complementarity. However, there is limited research on coupling heat pumps with energy storage to enhance system resilience. 2) Most existing research focuses on a single CET and GCT mechanism, with occasional literature studying the coupling mechanism between the two, but no solution has been proposed for the overlapping parts of the two mechanisms. 3) Although existing research has explored a series of uncertainty mitigation methods, it is limited to studying the operational characteristics of the energy storage devices themselves and has not coupled the response capabilities of the devices with the fluctuation characteristics of the system, making it difficult to effectively explore the response capabilities of multiple devices.

Based on the above research, this paper proposes optimized scheduling of a heat pump energy storage coupling system considering carbon certification's synergy and response characteristics. Compared with existing research, it has the following innovative points:

(1) A coupling system consisting of a heat pump unit and a thermal storage device has been constructed, and a flexible adjustment mechanism for an electric thermal integrated energy system has been proposed to effectively improve its energy utilization efficiency.

(2) Established a collaborative mechanism for carbon certification and proposed a solution for duplicate accounting between the CET and GCT mechanisms. The two mechanisms complement each other, effectively controlling carbon emissions and improving clean energy consumption.

(3) A response characteristic model based on the complete ensemble empirical mode decomposition with adaptive noise (CEEMDAN) was constructed, which consists of low-frequency components with small response frequency and large amplitude for medium and large equipment with high inertia and medium/high-frequency components with small response amplitude

and positive/negative periodic oscillation for energy storage equipment that requires repeated charging and discharging.

The other parts of this article consist of: Section 2, which constructs the operational framework and mathematical model of the heat pump energy storage coupling system. Section 3, where a carbon certification collaboration mechanism for a coupled system and a response characteristic model based on CEEMDAN-IIR was designed. Section 4, where an optimization scheduling model for heat pump energy storage coupling systems was constructed. Section 5, where a comprehensive energy system was taken as an example for numerical analysis, provides a reference for developing heat pumps and thermal storage equipment.

Framework of Heat Pump Energy Storage Coupling System

System Operation Framework

The source end of the heat pump energy storage coupling system constructed in this article consists of coal-fired power generation (CFG), photovoltaic power generation (PV), wind power generation (WP), and gas boiler (GB). The conversion end comprises power-to-gas (P2G) equipment and a ground source heat pump (GHP). The storage end includes a storage battery (SBA) and thermal storage equipment (TSE). The load side includes electrical, thermal, and natural gas loads. The operating framework of the coupled system is shown in Fig. 1.

As shown in Fig. 1, the coupling mechanism of the heat pump energy storage system is that the electrical load is satisfied by CFG, PV, WP, and SBA. GB, GHP, and TSE meet the heat load. The electricity-to-gas conversion equipment and the natural gas network meet the natural gas load. Excess electricity is stored in the SBA during periods of low energy consumption. If there is still surplus electricity, it is converted into heat energy through a GHP and stored in a TSE. During peak energy consumption periods, batteries and thermal storage devices discharge energy to meet both electrical and thermal loads, reducing the power consumption of GHP. In addition, the heat pump energy storage coupling system interacts with the external distribution network and participates in the green certificate and carbon trading market.

System Mathematical Modeling

CFG

The output of CFG units is related to coal consumption and power generation efficiency, as shown in Equation (1):
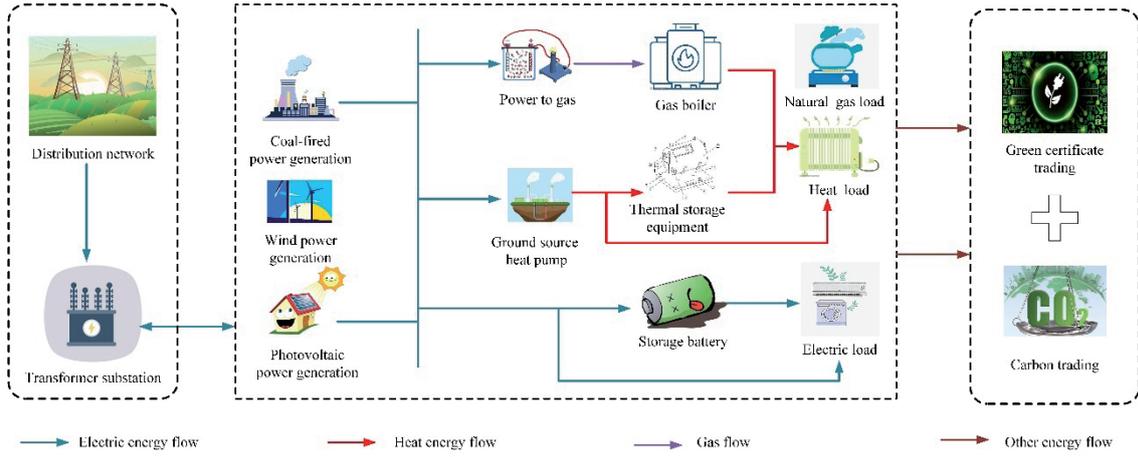
Fig. 1. System collaborative operation framework.

$$P_t^{\mathrm{CFG}} = \frac{\alpha^{\mathrm{CFG}} O_t^{\mathrm{CFG}}}{\theta_{\mathrm{coal}}} \quad (1)$$

Where, P_t^{CFG} is the output of the CFG unit at time t; α^{CFG} is the efficiency of CFG; O_t^{CFG} is the coal consumption of CFG units at time t; θ_{cola} is the lower calorific value of coal.

PV

The output of PV panels depends on the intensity of light radiation, and the relationship between output and radiation intensity is shown in Equation (2):

$$P_t^{\mathrm{PV}} = \alpha^{\mathrm{PV}} F_t^{\mathrm{PV}} S_t^{\mathrm{PV}} \quad (2)$$

Where, P_t^{PV} is the output of the photovoltaic panel at time t; α^{PV} and S_t^{PV} is the power generation efficiency and area of photovoltaic panels; F_t^{PV} is the intensity of light radiation at time t.

WP

The output of WP depends on the wind speed, and the relationship between output and wind speed is shown in Equation (3):

$$P_t^{\mathrm{WP}} = \begin{cases} 0 & v_t^{\mathrm{WP}} < v_{\mathrm{in}}^{\mathrm{WP}}, v_t^{\mathrm{WP}} > v_{\mathrm{out}}^{\mathrm{WP}} \\ P_e^{\mathrm{WP}} \cdot \dfrac{v_t^{\mathrm{WP}} - v_{\mathrm{in}}^{\mathrm{WP}}}{v_e^{\mathrm{WP}} - v_{\mathrm{in}}^{\mathrm{WP}}} & v_{\mathrm{in}}^{\mathrm{WP}} \le v_t^{\mathrm{WP}} < v_e^{\mathrm{WP}} \\ P_e^{\mathrm{WP}} & v_e^{\mathrm{WP}} \le v_t^{\mathrm{WP}} \le v_{\mathrm{out}}^{\mathrm{WP}} \end{cases} \quad (3)$$

Where, P_t^{WP} is the output of the WP at time t; P_e^{WP} is the rated output of the WP; v_t^{WP} is the wind speed at time t; $v_{\mathrm{in}}^{\mathrm{WP}}$, $v_{\mathrm{out}}^{\mathrm{WP}}$, and v_e^{WP} is the WP's inlet wind speed, outlet wind speed, and rated wind speed.

GB

The GB is a gas thermal coupling device, and its output model is shown in Equation (4):

$$H_t^{\mathrm{GB}} = \alpha^{\mathrm{GB}} G_{\mathrm{in},t}^{\mathrm{GB}} \quad (4)$$

Where, P_t^{GB} is the heat generation of the GB at time t; α^{GB} is the heat production efficiency of the GB; $G_{\mathrm{in},t}^{\mathrm{GB}}$ is the natural gas consumed by the GB at time t.

GHP

A typical HP unit comprises a compressor, condenser, evaporator, and thermal expansion valve. It extracts heat from the ground source by consuming electrical energy, recovering low-temperature heat sources to produce high-temperature heat sources. The schematic diagram of the ground source heat pump is shown in Fig. 2.

The output of the GHP is shown in Equation (5):

$$H_t^{\mathrm{HP}} = \alpha_{\mathrm{com}} \cdot \alpha_{\mathrm{con}} \cdot P_{\mathrm{in},t}^{\mathrm{HP}} \quad (5)$$

Where, H_t^{HP} is the heat generated by the HP at time t; α_{com} and α_{con} represents the efficiency of the compressor and condenser, respectively; $P_{\mathrm{in},t}^{\mathrm{HP}}$ is the electrical energy consumed by the HP at time t.

P2G

The electric-to-gas conversion equipment consists of two stages. The first stage is to generate hydrogen gas by electrolyzing water, and the second stage is to mix hydrogen gas with CO_2 to generate methane, as shown in Equation (6):
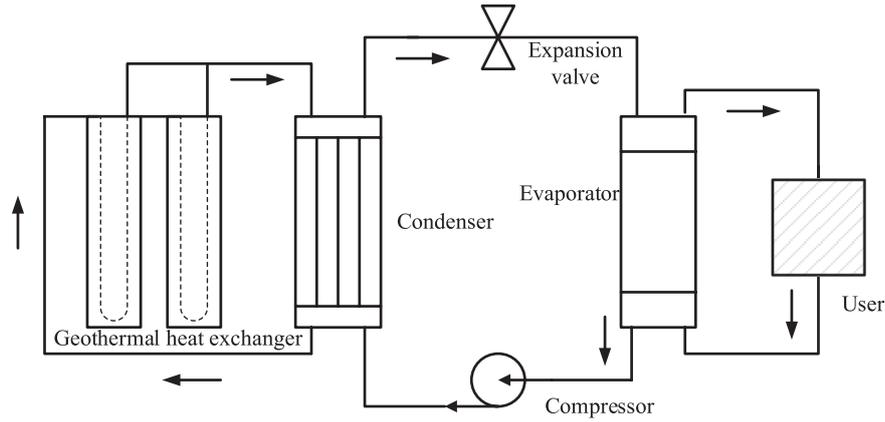
$$\begin{cases} 2H_2O \rightarrow 2H_2 + O_2 \\ 4H_2 + CO_2 \rightarrow CH_4 + 2H_2O \end{cases} \quad (6)$$
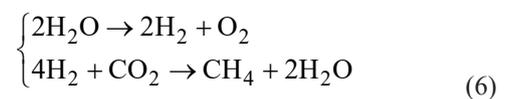
Fig. 2. Structure of GHP.

Based on this, the gas production of P2G equipment is obtained as shown in Equation (7):

$$G_t^{\text{P2G}} = \alpha_{\text{H}_2} \cdot \alpha_{\text{co}_2} \cdot P_{\text{in},t}^{\text{P2G}}$$

(7)

Where, G_t^{P2G} is the gas production of P2G equipment at time t; α_{H_2} and α_{CO_2} is the efficiency of the first and second stages of P2G conversion; $P_{\text{in},t}^{\text{P2G}}$ is the gas production rate of the P2G conversion equipment.

SBA

The battery discharges during peak hours and charges during valley hours, as shown in Equation (8):

$$Q_t^{\text{SBA}} = Q_{t-1}^{\text{SBA}}(1 - \alpha_{\text{loss}}^{\text{SBA}}) + \left(P_{\text{cha},t}^{\text{SBA}} \alpha_{\text{cha}}^{\text{SBA}} - \frac{P_{\text{dis},t}^{\text{SBA}}}{\alpha_{\text{dis}}^{\text{SBA}}} \right) \cdot \Delta t$$

(8)

Where, Q_t^{SBA} and Q_{t-1}^{SBA} is the capacity of the SBA at time t and t-1; $\alpha_{\text{loss}}^{\text{SBA}}$ is the self-loss rate of the SBA; $P_{\text{cha},t}^{\text{SBA}}$ and $P_{\text{dis},t}^{\text{SBA}}$ is the charging and discharging power of the SBA at time t; $\alpha_{\text{cha}}^{\text{SBA}}$ and $\alpha_{\text{dis}}^{\text{SBA}}$ is the charging and discharging efficiency of the SBA.

TSE

The TSE releases heat during peak hours and stores heat during valley hours, as shown in Equation (9):

$$Q_t^{\text{TSE}} = Q_{t-1}^{\text{TSE}}(1 - \alpha_{\text{loss}}^{\text{TSE}}) + \left(H_{\text{cha},t}^{\text{TSE}} \alpha_{\text{cha}}^{\text{TSE}} - \frac{H_{\text{dis},t}^{\text{TSE}}}{\alpha_{\text{dis}}^{\text{TSE}}} \right) \cdot \Delta t$$

(9)

Where, Q_t^{TSE} and Q_{t-1}^{TSE} is the capacity of the TSE at time t and t-1; $\alpha_{\text{loss}}^{\text{TSE}}$ is the self-loss rate of the TSE;

$H_{\text{cha},t}^{\text{TSE}}$ and $H_{\text{dis},t}^{\text{TSE}}$ is the heat storage and release power of the TSE at time t; $\alpha_{\text{cha}}^{\text{TSE}}$ and $\alpha_{\text{dis}}^{\text{TSE}}$ is the heat storage and release efficiency of the TSE.

Material and Methods

Analysis of the Carbon Certification Collaboration Mechanism and Response Characteristics

Carbon Certification Collaborative Mechanism

The carbon certification collaborative mechanism refers to the coordinated participation of heat pump coupling systems in the CET and GCT markets. Below, we will elaborate on the two markets separately and construct a collaborative mechanism.

(1) CET

CET refers to the situation where if the actual CO_2 emissions of an accounting entity exceed the free allocation of carbon emissions, the accounting entity needs to purchase the missing carbon emission rights in the carbon trading market. Otherwise, the excess carbon emissions can be sold in the carbon trading market. This paper uses benchmark values to determine the free carbon emissions, and based on this, the net emissions of the heat pump energy storage coupling system are obtained as shown in Equation (10):

$$\begin{cases} D_{\text{co}_2,t}^{\text{free}} = d_{\text{co}_2}^{\text{e}} \left(P_t^{\text{CFP}} + P_t^{\text{pv}} + P_t^{\text{WP}} \right) + d_{\text{co}_2}^{\text{h}} \left(H_t^{\text{HP}} + H_t^{\text{GB}} \right) \\ D_{\text{co}_2,t}^{\text{ac}} = d_{\text{co}_2}^{\text{CFP}} \left(P_t^{\text{CFP}} + P_{\text{buy},t}^{\text{grid}} \right) + + d_{\text{co}_2}^{\text{GB}} H_t^{\text{GB}} \\ D_{\text{co}_2,t}^{\Delta \text{ac}} = D_{\text{co}_2,t}^{\text{free}} - D_{\text{co}_2,t}^{\text{ac}} \end{cases}$$

(10)

Where, $D_{\text{co}_2,t}^{\text{free}}$, $D_{\text{co}_2,t}^{\text{ac}}$, and $D_{\text{co}_2,t}^{\Delta \text{ac}}$ is the free carbon quota, actual carbon emissions, and net carbon emissions of the coupled system at time t; $d_{\text{co}_2}^{\text{e}}$

and $d_{co_2}^h$ is the free carbon quota coefficient for unit electricity and heat energy; $d_{co_2}^{CFP}$ and H_t^{GB} is the carbon emissions per unit of CFG and gas-fired boiler output, respectively.

Introducing a tiered carbon price in the CET obtains the carbon trading cost of the heat pump energy storage coupling system, as shown in Equation (11). If $D_{co_2,t}^{\Delta ac} > 0$, the carbon trading cost of the coupling system is $-\left|C_t^{CTM}\right|$, otherwise, it is $\left|C_t^{CTM}\right|$.

$$
\left|C_t^{CTM}\right| = \begin{cases} \left|D_{co_2,t}^{\Delta ac}\right| \cdot \overline{u}_{co_2}^{base} & \left|D_{co_2,t}^{\Delta ac}\right| \leq g \\ g \cdot \overline{u}_{co_2}^{base} + \overline{u}_{co_2}^{base} \cdot \left(1 + \gamma^{cr}\right)\left(\left|D_{co_2,t}^{\Delta ac}\right| - g\right) & g < \left|D_{co_2,t}^{\Delta ac}\right| \leq 2g \\ g \cdot \left(2 + \gamma^{cr}\right) \cdot \overline{u}_{co_2}^{base} + \overline{u}_{co_2}^{base} \cdot \left(1 + 2\gamma^{cr}\right) \cdot \left(\left|D_{co_2,t}^{\Delta ac}\right| - 2g\right) & 2g < \left|D_{co_2,t}^{\Delta ac}\right| \leq 3g \\ g \cdot \left(3 + 3\gamma^{cr}\right) \cdot \overline{u}_{co_2}^{base} + \overline{u}_{co_2}^{base} \cdot \left(1 + 3\gamma^{cr}\right) \cdot \left(\left|D_{co_2,t}^{\Delta ac}\right| - 3g\right) & 3g < \left|D_{co_2,t}^{\Delta ac}\right| \leq 4g \end{cases}
$$
(11)

Where, $\overline{u}_{co_2}^{base}$ is the benchmark price for CO_2 trading; g is the range of carbon emissions; γ^{cr} s the growth rate of carbon emission trading prices.

(2) GCT

GCT refers to the regulation that in order to promote the development of renewable energy, the amount of renewable energy generated in a certain system cannot be less than a certain value. If the number of green certificates in a system is less than the specified value, purchasing the missing green certificates in the GCT market is necessary. If the number of green certificates in the system exceeds the specified value, excess green certificates need to be sold in the GCT market. The green certificate source for the heat pump energy storage coupling system is photovoltaic power generation. The net green certificate number of the coupled system can be obtained as shown in Equation (12):

$$
\begin{cases} D_{CET,t}^{ex} = d_{CET}^{ex}\left(L_t^{ele} + L_t^{heat}\right) \\ D_{CET,t}^{ac} = D_{CET} \cdot \left(P_t^{pv} + P_t^{WP}\right) \\ D_{CET,t}^{\Delta ac} = D_{CET,t}^{ac} - D_{CET,t}^{ex} \end{cases}
$$
(12)

Where, $D_{CET,t}^{ex}$ and $D_{CET,t}^{ac}$ represents the number of green certificates specified and actual at time t, respectively; d_{CET}^{ex} is the minimum holding amount of green certificates per unit load; $D_{CET,t}^{\Delta ac}$ is the net number of green certificates at time t.

Based on Equation (12), the green certificate transaction cost of the heat pump energy storage coupling system is obtained as shown in Equation (13). If $D_{CET,t}^{\Delta ac} > 0$, the green certificate transaction cost is $-\left|C_t^{CET}\right|$, otherwise it is $\left|C_t^{CET}\right|$.

$$
\left|C_t^{CET}\right| = D_{CET,t}^{\Delta ac} \cdot \overline{u}_t^{CET}
$$
(13)

Where, $\overline{u}_t^{CET}$ is the unit green certificate price.

(3) Carbon certification collaborative mechanism

Photovoltaic power generation in the coupled system not only calculates free carbon quotas in carbon trading but also calculates the number of green certificates in the GCT mechanism. In order to avoid duplicate calculations, this paper uses the average method to subtract duplicate parts, and the resulting kernel reduction is shown in Equation (14):

$$
C_t^{\Delta CGM} = \frac{\left(\overline{u}_{co_2}^{base} + \overline{u}_t^{CET}\right) \cdot \left(P_t^{pv} + P_t^{WP}\right)}{2}
$$
(14)

Where, $C_t^{\Delta CGM}$ is the cost reduction under the carbon certification collaborative mechanism.

Analysis of Response Characteristics Based on CEEMDAN-IIR

(1) Analysis framework diagram

In order to match the differences in response characteristics of different devices and reduce the uncertainty between the source and load ends of the coupled system, where the uncertainty at the source end comes from photovoltaic output and the uncertainty at the load end comes from electricity, heat, and natural gas loads. Based on this, this paper decomposes photovoltaic output, electrical load, thermal load, and natural gas load into low-frequency, mid-frequency, and high-frequency components using the CEEMDAN-IIR method.

In optimizing low-frequency components, the low-frequency components are input as basic parameters into the model, and the objective function is to minimize the comprehensive cost to obtain the initial output of GB, GHP, P2G, and CFG units. In optimizing intermediate frequency components, the objective function is to minimize the comprehensive cost and optimize SBA and TSE's charging and discharging plans. In high-frequency component optimization, the objective is to minimize the overall cost and optimize the charging and discharging adjustment plan for SBA and TSE. The specific optimization framework is shown in Fig. 3.

(2) CEEMDAN-IIR

The empirical mode decomposition (EMD) method, as the most commonly used method for signal decomposition, essentially decomposes the original signal into a series of intrinsic mode functions (IMFs) with different amplitudes by varying the scales of the fluctuations. The Complete Ensemble Empirical Mode Decomposition with Adaptive Noise (CEEMDAN) algorithm is an improved empirical mode decomposition method. The CEEMDAN algorithm can reduce the reconstruction error to almost zero with fewer average
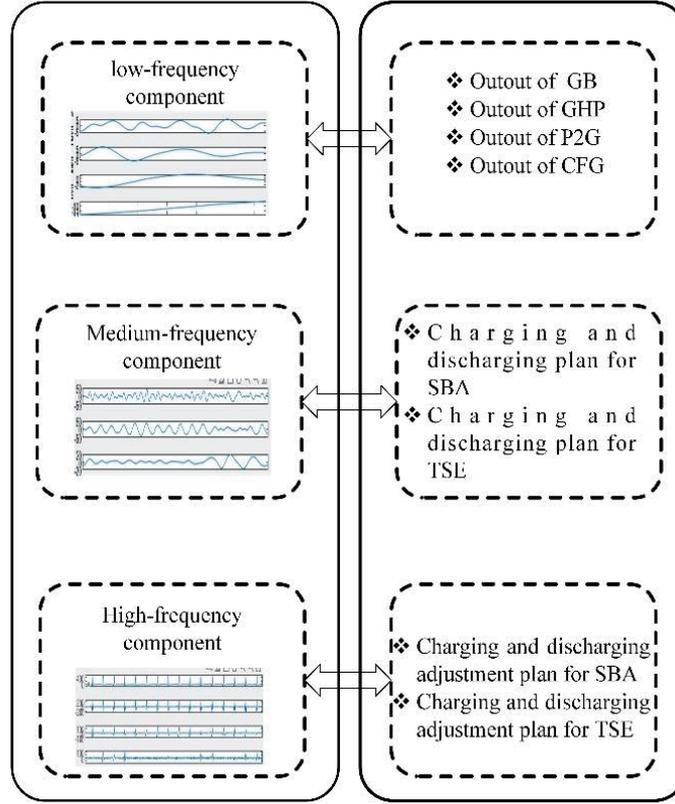
Fig. 3. Optimization framework.

iterations by adding a finite number of adaptive white noises at each stage, effectively avoiding the mode aliasing problem of EMD methods.

However, the number of IMF components obtained by CEEMDAN decomposition is too large, and the frequency distribution of each IMF component does not strictly conform to the time scale divided in the previous text, so it is necessary to reconstruct each fluctuation component. This paper uses an infinite impulse response (IIR) filter to decompose and reconstruct the IMF components in the three frequency bands mentioned above, obtaining the fluctuation components of photovoltaic output, electrical load, thermal load, and natural gas load at three time scales: high frequency (<15 minutes), medium frequency (15-60 minutes), and low frequency (>1 hour). Taking photovoltaic output as an example, a signal decomposition model is constructed, and the signal decomposition steps of the load are consistent with photovoltaic output.

1) CEEMDAN algorithm

Suppose P is defined as the original sequence of photovoltaic output, and $IMF_i(1, 2, , ..., n)$ and *res* are the individual fluctuation components and residuals decomposed by the CEEMDAN algorithm. In this case, the relationship is as shown in Equation (15):

$$P = \sum_{i=1}^{n} IMF_i + res \tag{15}$$

Where the magnitude of *res* is relatively small and can be ignored.

2) IIRF algorithm

Firstly, an IIR low-pass filter separates the low-frequency components from each IMF component.

$$IMF_i = IMF_i^{low} + IMF_i^{rest} \tag{16}$$

Where, IMF_i^{low} and IMF_i^{rest} represents the low-frequency and residual parts of the IMF component.

Then, an IIR high-pass filter separates the high-frequency components from the remaining parts of each IMF component.

$$IMF_i^{rest} = IMF_i^{high} + IMF_i^{mid} \tag{17}$$

Where, IMF_i^{high} is the high-frequency part of the i-th IMF component; the remaining IMF_i^{mid} is the intermediate frequency part of the i-th IMF component.

Finally, reconstruct according to different frequency distributions.

$$\begin{cases} F_{low} = \sum_{i=1}^{n} IMF_i^{low} \\ F_{mid} = \sum_{i=1}^{n} IMF_i^{mid} \\ F_{high} = \sum_{i=1}^{n} IMF_i^{high} \end{cases} \tag{18}$$

Where, F_{high}, F_{mid} and F_{low} refers to the high-frequency component (<15 minutes), mid-frequency component (15-60 minutes), and low-frequency component (>1 hour) of the net load.

Optimization and Scheduling Model of Heat Pump Energy Storage Coupling System

Objective Function

In order to balance economy and environmental protection, the economic aspect is characterized by the minimum total cost of the coupled system, while the environmental aspect is characterized by the maximum renewable energy consumption rate.

(1) Minimize total cost

The cost of a heat pump energy storage coupling system consists of the operating cost of the equipment, carbon certificate trading cost, external interaction cost, penalty cost for wind and solar power curtailment, and energy sales revenue, as shown in Equation (19):

$$C^{total} = \sum_{t=1}^{24} \left(C_t^{op} + C_t^{grid} + C_t^{CTM} + C_t^{CET} + \Delta C_t^{\Delta CGM} + C_t^{pun} - R_t^{sale} \right) \tag{19}$$

Where, C^{total} is the total cost of the coupled system; C_t^{op}, C_t^{grid}, C_t^{pun}, and R_t^{sale} is the operating cost, external interaction cost, wind and solar curtailment penalty cost, and energy sales revenue of the coupled system at time t.

The operating cost of the system is shown in Equation (20):

$$\min C_t^{op} = \min \begin{pmatrix} \overline{u}_{pv}^{op} \cdot P_t^{pv} + \overline{u}_{WP}^{op} \cdot P_t^{WP} + \overline{u}_{SBA}^{op} \left(P_{cha,t}^{SBA} + P_{dis,t}^{SBA} \right) + \overline{u}_{CFG}^{op} \cdot P_t^{CFG} + \\ \overline{u}_{GB}^{op} \cdot H_t^{GB} + \overline{u}_{HP}^{op} H_t^{HP} + \overline{u}_{TSE}^{op} \left(H_{cha,t}^{TSE} + H_{dis,t}^{TSE} \right) + \overline{u}_{P2G}^{op} \cdot G_t^{P2G} \end{pmatrix} \tag{20}$$

Where, $\overline{u}_{pv}^{op}$, $\overline{u}_{WP}^{op}$, $\overline{u}_{SBA}^{op}$, $\overline{u}_{CFG}^{op}$, $\overline{u}_{GB}^{op}$, $\overline{u}_{HP}^{op}$, $\overline{u}_{TSE}^{op}$, and $\overline{u}_{P2G}^{op}$ represents the unit operating costs of PV, WP, SBA, CFG, GB, HP, TSE, and P2G, respectively.

The external interaction cost is the cost generated by the interaction between the coupled system and the power grid, heating network, and natural gas network, as shown in Equation (21):

$$C_t^{grid} = u_{e,t}^{grid} \left(P_{buy,t}^{grid} - P_{sale,t}^{grid} \right) + u_{h,t}^{grid} \left(H_{buy,t}^{grid} - H_{sale,t}^{grid} \right) + u_{g,t}^{grid} \left(G_{buy,t}^{grid} - G_{sale,t}^{grid} \right) \tag{21}$$

Where, $u_{e,t}^{grid}$, $u_{h,t}^{grid}$, and $u_{g,t}^{grid}$ is the interaction cost between the coupled system at time t and the power grid, heating network, and natural gas network; $P_{buy,t}^{grid}$ and $P_{sale,t}^{grid}$ is the purchase and sales volume of the coupled system at time t on the power grid; $H_{buy,t}^{grid}$ and $H_{sale,t}^{grid}$ is the purchase and sales volume of the coupled system at the heating network at time t; $G_{buy,t}^{grid}$ and $G_{sale,t}^{grid}$ is the purchase and sales volume of the coupled system at time t in the natural gas network, respectively.

The cost of wind and solar curtailment penalty is the cost caused by the uncertainty of clean energy output in the coupled system, as shown in Equation (22):

$$C_t^{pun} = u_{re}^{pun} \cdot \left(\left| P_t^{pv} - P_t^{pre,pv} \right| + \left| P_t^{WP} - P_t^{pre,WP} \right| \right) \tag{22}$$

Where, u_{re}^{pun} is the uncertainty cost caused by the error in unit clean energy output; $P_t^{pre,pv}$ and $P_t^{pre,WP}$ is the predicted output of photovoltaic and wind power generation at time t.

Energy sales revenue refers to the income obtained by the system through the sale of electricity, heat, and natural gas, as shown in Equation (23):

$$R_t^{sale} = \sum_{i \in I} L_t^i \cdot u_{sale,t}^i \tag{23}$$

Where, $u_{sale,t}^i$ is the unit income of the i-th energy source.

(2) Maximum renewable energy consumption rate

The clean energy consumption rate is shown in Equation (24):

$$\max \ell_{re} = \max \left(\frac{P_{ac,t}^{PV} + P_{ac,t}^{WP}}{P_t^{PV} + P_t^{WP}} \right) \tag{24}$$

Where, ℓ_{re} is renewable energy consumption rate; $P_{ac,t}^{PV}$ and $P_{ac,t}^{WP}$ is the actual output of PV and WP.

Constraints

The operation of the heat pump energy storage coupling system is subject to constraints such as balance, operation, external interaction, and climbing, among which the system balance constraints include electrical energy, thermal energy, and natural gas balance constraints, as shown in Equation (25):

$$\begin{cases} P_t^{pv} + P_t^{WP} + P_{dis,t}^{SBA} + P_t^{CFG} + P_{buy,t}^{grid} = P_{sale,t}^{grid} + P_{cha,t}^{SBA} + P_{in,t}^{HP} + P_{in,t}^{P2G} + L_t^{ele} \\ H_t^{GB} + H_t^{HP} + H_{dis,t}^{TSE} + H_{buy,t}^{grid} = H_{sale,t}^{grid} + H_{cha,t}^{TSE} + L_t^{heat} \\ G_t^{P2G} + G_{buy,t}^{grid} = G_{sale,t}^{grid} + G_{in,t}^{GB} \end{cases}$$

$$(25)$$

The operational constraints of the coupled system are shown in Equation (26):

$$\begin{cases} P_{min}^{pv} \leq P_t^{pv} \leq P_{max}^{pv} \\ P_{min}^{WP} \leq P_t^{WP} \leq P_{max}^{WP} \\ P_{min}^{CFG} \leq P_t^{CFG} \leq P_{max}^{CFG} \\ H_{min}^{GB} \leq H_t^{GB} \leq H_{max}^{GB} \\ H_{min}^{HP} \leq H_t^{HP} \leq H_{max}^{HP} \\ G_{min}^{P2G} \leq G_t^{P2G} \leq G_{max}^{P2G} \end{cases}$$

$$(26)$$

Where, P_{min}^{pv} and P_{max}^{pv} is the minimum and maximum value of PV output; P_{min}^{WP} and P_{max}^{WP} is the minimum and maximum value of WP output; P_{min}^{CFG} and P_{max}^{CFG} is the minimum and maximum value of CFG output; H_{min}^{GB} and H_{max}^{GB} is the minimum and maximum value of GB output; H_{min}^{HP} and H_{max}^{HP} is the minimum and maximum value of HP output; G_{min}^{P2G} and G_{max}^{P2G} is the minimum and maximum value of P2G output.

The operational constraints of SBA and TSE are shown in Equations (27) and (28), respectively:

$$\begin{cases} P_{min}^{SBA} \leq P_{cha,t}^{SBA}, P_{dis,t}^{SBA} \leq P_{max}^{SBA} \\ P_{cha,t}^{SBA} \cdot P_{dis,t}^{SBA} = 0 \\ Q_1^{SBA} = Q_{24}^{SBA} \\ Q_{min}^{SBA} \leq Q_t^{SBA} \leq Q_{max}^{SBA} \end{cases}$$

$$(27)$$

$$\begin{cases} H_{min}^{TSE} \leq H_{cha,t}^{TSE}, H_{dis,t}^{TSE} \leq H_{max}^{TSE} \\ H_{cha,t}^{TSE} \cdot H_{dis,t}^{TSE} = 0 \\ Q_1^{TSE} = Q_{24}^{TSE} \\ Q_{min}^{TSE} \leq Q_t^{TSE} \leq Q_{max}^{TSE} \end{cases}$$

$$(28)$$

Where, P_{min}^{SBA} and P_{max}^{SBA} represents the minimum and maximum values of SBA charging and discharging power; Q_1^{SBA} and Q_{24}^{SBA} is the capacity of SBA at the 1st and 24th moments; Q_{min}^{SBA} and Q_{max}^{SBA} is the minimum and maximum values of SBA capacity; H_{min}^{TSE} and H_{max}^{TSE} represents the minimum and maximum values of TSE charging and discharging power; Q_1^{TSE}

and Q_{24}^{TSE} is the capacity at the 1st and 24th moments of TSE; Q_{min}^{TSE} and Q_{max}^{TSE} represents the minimum and maximum values of TSE capacity.

The specific external interaction constraints are shown in Equation (29):

$$\begin{cases} P_{buy,t}^{grid} \cdot P_{sale,t}^{grid} = 0 \\ H_{buy,t}^{grid} \cdot H_{sale,t}^{grid} = 0 \\ G_{buy,t}^{grid} \cdot G_{sale,t}^{grid} = 0 \end{cases}$$

$$(29)$$

Results and Discussion

Basic Data

This paper takes a heat pump energy storage coupling system in a certain region as an example to conduct a numerical analysis. The operating parameters and economic parameters of each device in the coupling system are shown in Table 1 [21-24].

The interaction prices between the coupling system and the external power grid, heating network, and natural gas network are all based on time-of-use electricity prices, as shown in Table 2 [25].

The prices of electricity, heat, and gas sales within the coupling system are shown in Table 3.

The interaction limits between the coupling system and the power grid and between the heating network and the gas grid are set to 500 kW, 800 kW, and 10 m³, respectively. The limits for other units are shown in Table 4:

The summer predicted output of wind power generation and photovoltaic power generation is shown in Fig. 4.

The summer demand for electricity, heat, and gas loads is shown in Fig. 5.

Results Analysis

Optimization Result Analysis

(1) Signal decomposition results

The signal decomposition of wind power output, photovoltaic output, electricity load demand, heat load demand, and natural gas load demand based on Equations (15) - (18) is shown in Fig. 6.

Fig. 6 shows that in terms of fluctuation amplitude, the low-frequency component>the mid-frequency component>the high-frequency component. Based on the decomposition results of the photovoltaic output, the fluctuation amplitudes of low-frequency, mid-frequency, and high-frequency components are within the range of [01000kW], [-400400] kW, and [-100100] kW. This indicates that the amplitude of low-frequency

Table 1. Operational and economic parameters.

Parameter	Value of parameter	Parameter	Value of parameter	Parameter	Value of parameter	Parameter	Value of parameter
α^{CFG}	0.88	θ_{coal}	29271.2 kJ/kg	α^{GB}	0.85	α_{com}	0.90
α_{con}	0.90	α_{H_2}	0.80	α_{co_2}	0.90	α_{loss}^{SBA}	0.1%/day
α_{cha}^{SBA}	90%	α_{dis}^{SBA}	90%	α_{loss}^{TSE}	0.1%/day	α_{cha}^{TSE}	95%
α_{dis}^{TSE}	95%	$d_{co_2}^{e}$	0.8 kg/kWh	$d_{co_2}^{h}$	0.6 kg/kWh	$\overline{u}_{co_2}^{base}$	130 Yuan/ton
g	800 kg	γ^{cr}	14%	d_{CET}^{ex}	0.2	$\overline{u}_{t}^{CET}$	0.08 Yuan /kWh
$\overline{u}_{pv}^{op}$	0.04 Yuan/kWh	$\overline{u}_{SBA}^{op}$	0.01 Yuan/kWh	$\overline{u}_{CFG}^{op}$	0.75 Yuan /kWh	$\overline{u}_{GB}^{op}$	0.35 Yuan/kWh
$\overline{u}_{HP}^{op}$	0.30 Yuan/kWh	$\overline{u}_{TSE}^{op}$	0.08 Yuan/kWh	$\overline{u}_{P2G}^{op}$	0.10 Yuan /kWh	u_{pv}^{pun}	0.1 Yuan /kWh

Table 2. External interaction price.

	Electricity selling price		Heat selling price		Gas selling price	
	Period of time	Price (Yuan/kWh)	Period of time	Price (Yuan/kWh)	Period of time	Price (Yuan/m³)
Peak	11:00-14:00 18:00-22:00	0.85	11:00-14:00 18:00-22:00	0.75	11:00-14:00 18:00-22:00	2.5
Flat	7:00-10:00 15:00-17:00	0.60	7:00-10:00 15:00-17:00	0.55	7:00-10:00 15:00-17:00	2.3
Valley	23:00-6:00	0.30	23:00-6:00	0.25	23:00-6:00	2.1

Table 3. Internal energy sales price.

	Electricity selling price		Heat selling price		Gas selling price	
	Period of time	Price (Yuan/kWh)	Period of time	Price (Yuan/kWh)	Period of time	Price (Yuan/m³)
Peak	11:00-14:00 18:00-22:00	0.95	11:00-14:00 18:00-22:00	0.85	11:00-14:00 18:00-22:00	2.6
Flat	7:00-10:00 15:00-17:00	0.70	7:00-10:00 15:00-17:00	0.65	7:00-10:00 15:00-17:00	2.4
Valley	23:00-6:00	0.40	23:00-6:00	0.35	23:00-6:00	2.2

Table 4. Unit capacity limit.

Unit	Maximum	Unit	Maximum	Unit	Maximum	Unit	Maximum
PV	1800kW	WP	3000kW	GB	100kW	HP	300kW
P2G	36m³	SBA	250kW	TSE	60kW	CFG	550kW

component fluctuations is relatively large, which can effectively match the operating characteristics of equipment such as GB, GHP, P2G, and CFG units. The high-frequency components oscillate periodically and have small fluctuation amplitudes, which is in line with the charging and discharging characteristics of SBA and TSE. It can reduce the operating state of energy storage devices that are overcharged or overdischarged

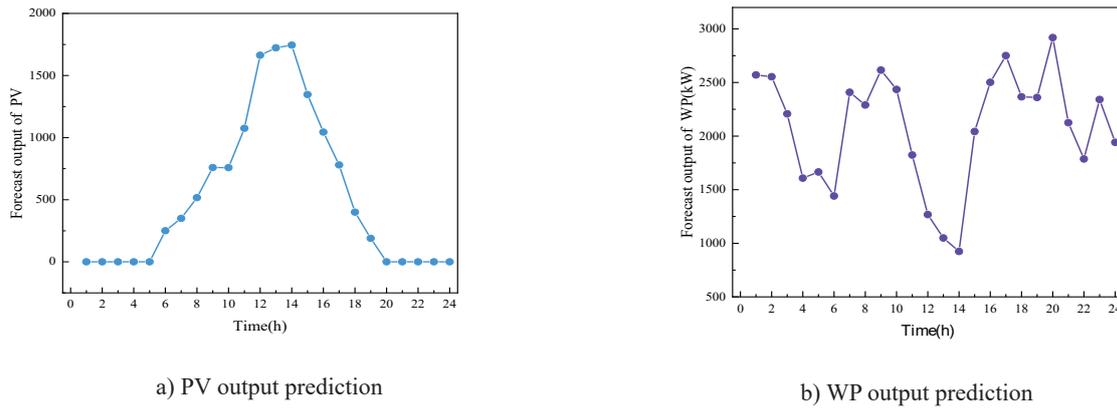a) PV output prediction

b) WP output prediction

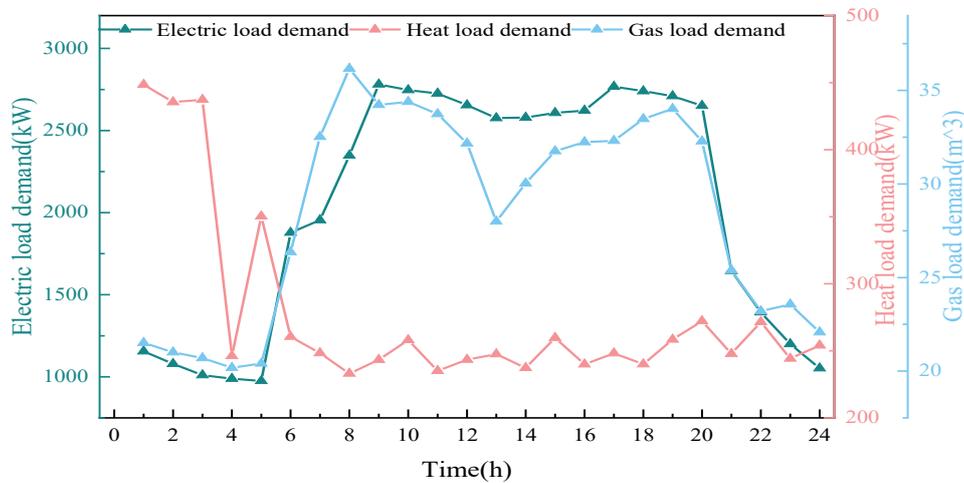Fig. 4. Predictive output of WP and PV.

Fig. 5. Load demand.

in a short period of time and improve the utilization rate of energy storage devices. From the comparison of the fluctuation amplitudes of various types of wind power generation and photovoltaic power generation, it can be seen that the fluctuation amplitude of wind power generation is greater than that of photovoltaic power generation, indicating that the volatility brought by wind power generation needs to be given special attention.

(2) System operation optimization results

Optimize and analyze the electrical, thermal, and natural gas subsystems of the heat pump energy storage coupling system based on the signal decomposition results. The operation optimization results of the electric energy subsystem are shown in Fig. 7.

From Fig. 7, it can be seen that wind power output and photovoltaic output have complementary characteristics. From 23:00 to 3:00, photovoltaic output was 0, but WP is in a high incidence stage. During 12:00-14:00, photovoltaic output peaked, while wind power output was relatively low. From 22:00 to 5:00, due to the high frequency of wind power generation, there is less demand for electricity load. After meeting the system's energy demand, the excess electricity

supply is stored in the SBA. During the time period of 1:00-3:00, after reaching the maximum storage capacity of the battery, the coupling system sells excess electricity to the external power grid. During 18:00-20:00, photovoltaic output was almost zero, and energy consumption peaked. Wind power alone cannot meet the system's energy demand, so coal-fired power generation units are started for energy supply.

The operation optimization results of the heat energy subsystem are shown in Fig. 8.

As shown in Fig. 8, the heat load demand of the heat pump energy storage coupling system is mainly met by the HP and the GB, with the heat generated by the heat pump being greater than that of the GB. This is mainly because HP's conversion efficiency is higher than that of GB. The TSE played a role in various time periods, including 15:00-17:00, 23:00-24:00, and 4:00. The TSE stores heat, and during these time periods, there is a sufficient supply of electrical energy. Part of the remaining electrical energy is converted into thermal energy through an HP and stored in the TSE. During the rest of the time, the heat storage equipment releases heat, especially from 1:00 to 3:00. The heat load

a) Decomposition of PV output signal

b) Decomposition of WP output signal

c) Decomposition of electric load output signal

d) Decomposition of heat load output Signal
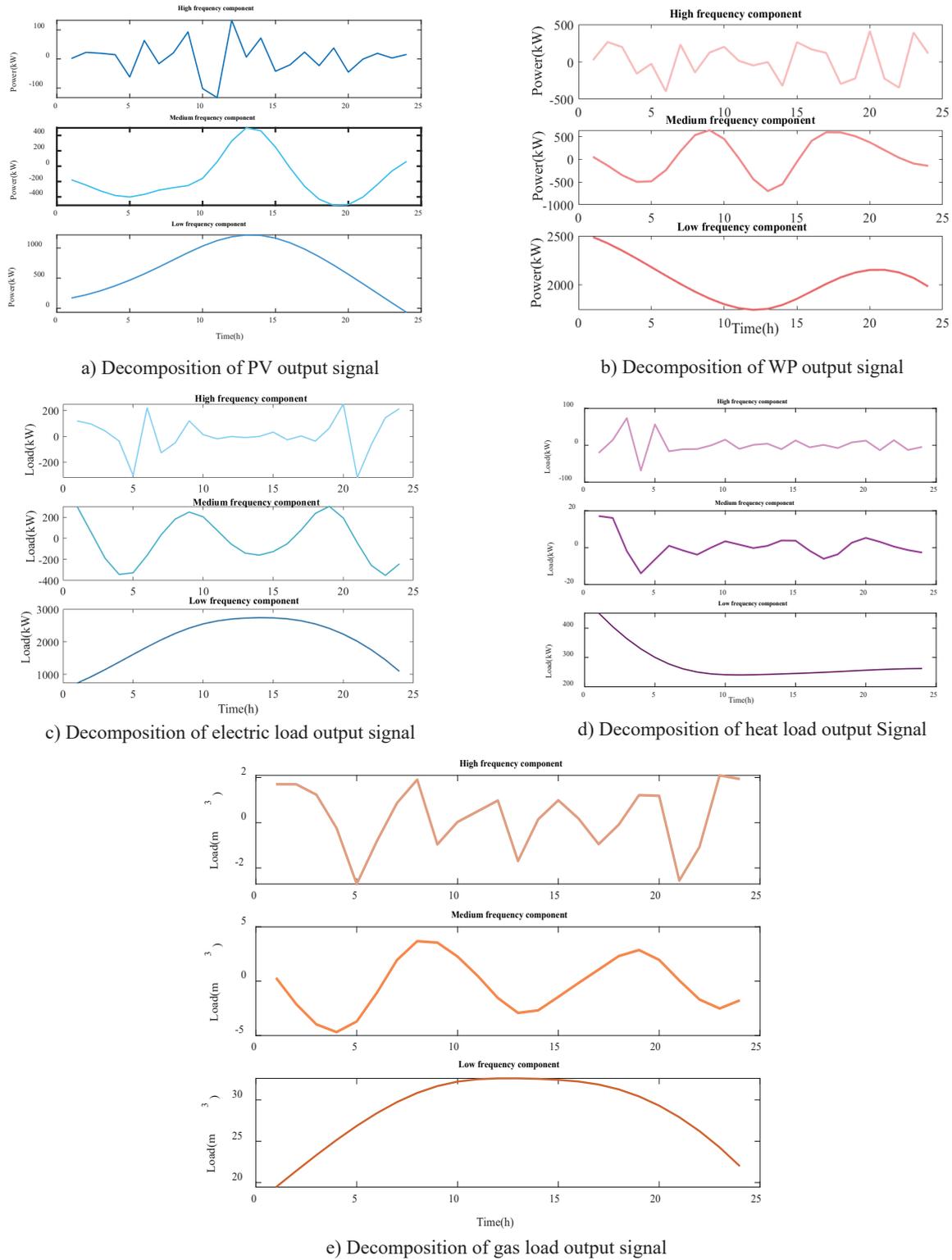

e) Decomposition of gas load output signal

Fig. 6. Signal decomposition results.

demand is high, and even after the heat pump operates at full power, it still cannot meet the heat load demand. It is necessary to use the TSE and externally purchased heat energy to meet the shortfall in heat demand. This indicates that the TSE effectively realizes the coupling between the electrical energy subsystem and the heat energy system.

The operation optimization results of the natural gas system are shown in Fig. 9.

As shown in Fig. 9, during the time periods of 2:00-3:00 and 5:00-7:00, it is necessary to supply both natural gas load demand and GB. Therefore, during these time periods, the natural gas generated by P2G equipment cannot meet the system's demand, and the system
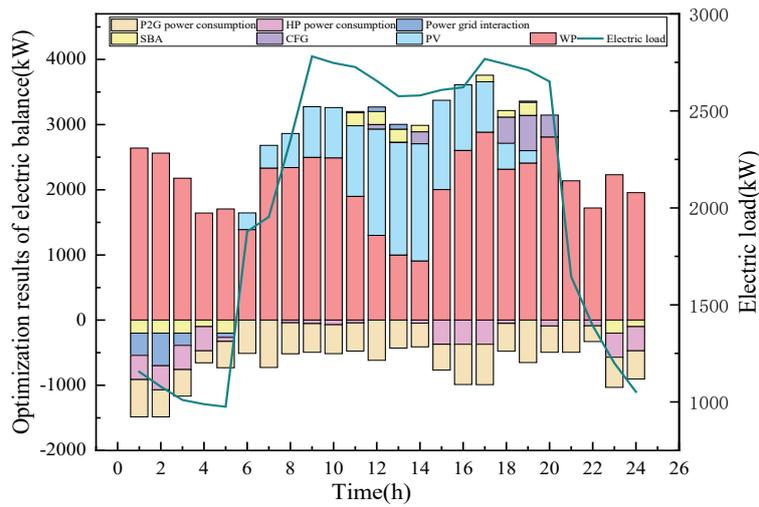
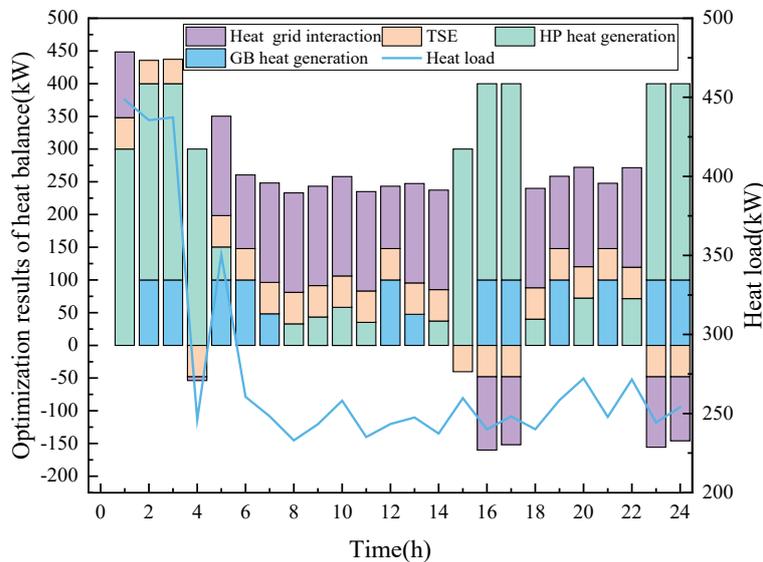Fig. 7. Optimization results of electric energy subsystem operation.

Fig. 8. Optimization results of heat energy subsystem operation.

needs to interact with the external natural gas network to purchase the missing natural gas. At the two time points of 1:00 and 7:00, there is an excess supply of natural gas, and the heat pump energy storage coupling system sells natural gas to the external natural gas network.

Effectiveness Analysis

This article's three innovative points are: the construction of a heat pump energy storage coupling system, the carbon certification collaborative mechanism, and the uncertainty decomposition of the CEEMDAN algorithm. It also analyzes the effectiveness of these three aspects.

(1) Effectiveness analysis of heat pump energy storage coupling system

In order to verify the effectiveness of the heat pump energy storage coupling system, three scenarios were set up, as shown in Table 5.

Based on the three scenarios set in Table 5, the operating costs and external interaction costs of the heat pump energy storage coupling system in the three scenarios are shown in Table 6.

According to Table 6, although the operating cost of Scenario 2 increased by 11.21 yuan compared to Scenario 1, the external interaction cost decreased by 428.89 yuan, with a reduction rate of 22.50%. This is because scenario 2 adds a thermal storage device based on scenario 1, increasing the operating cost of the TSE. However, through the thermal storage device's peak heat release and valley heat storage mechanism, it is possible to reduce the system's high-priced purchase of thermal energy during peak hours and lower the system's
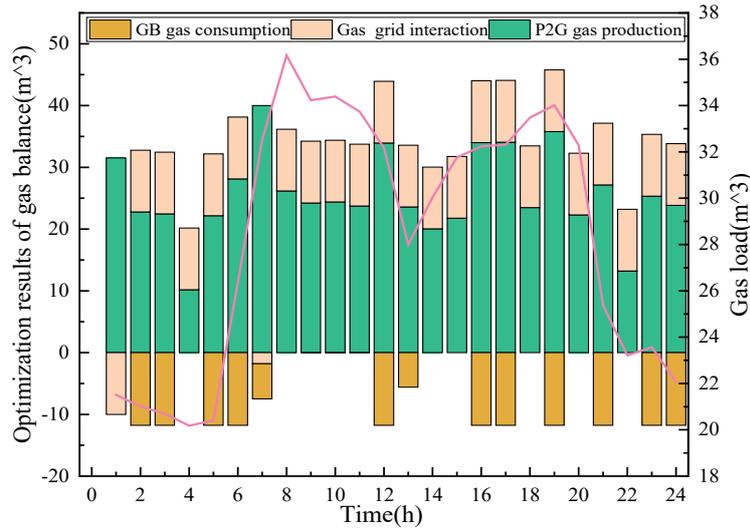
Fig. 9. Optimization results of natural gas subsystem operation.

Table 5. Scenario setting for effectiveness analysis of heat pump energy storage coupling system.

	Scenario 1	Scenario 2	Scenario 3
HP	×	×	√
TSE	×	√	√

Table 6. Scenario comparison of effectiveness analysis of heat pump energy storage coupling system.

	Scenario 1	Scenario 2	Scenario 3
Operating cost (yuan)	7625.35	7636.56	7167.12
External interaction cost (yuan)	1906.20	1477.31	1477.31

external interaction costs. Compared with Scenario 2, Scenario 3 has reduced operating costs by 469.44 yuan, with a reduction rate of 6.14%, and the external interaction costs are consistent. This is because scenario 3 is based on scenario 1, and the economic efficiency of heat generation through HP units is higher than that of GB, which can reduce the system's heat production cost.

(2) Analysis of the effectiveness of carbon certification collaboration mechanism

In order to verify the effectiveness of the carbon certification collaborative mechanism, the following three scenarios were set up:

Scenario 1: The coupled system only considers the CET;

Scenario 2: The coupled system only considers the GCT;

Scenario 3: The coupling system considers the carbon certification collaborative mechanism.

On this basis, the clean energy consumption rate and carbon dioxide emissions for the three scenarios are shown in Fig. 10.

According to Fig. 10, Scenario 1 has higher carbon dioxide emissions of 20.48kg and a lower clean energy consumption rate of 1.32% compared to Scenario 3. This is because Scenario 1 did not consider the GCT mechanism, resulting in a decrease in the driving force of the heat pump energy storage coupling system to absorb wind and photovoltaic power, leading to a decrease in the clean energy consumption rate. Under the condition of fixed load demand in the coupled system, the proportion of WP and PV output decreases while the proportion of CFP increases accordingly. Scenario 2 shows a 79.71% increase in carbon dioxide emissions and a 0.64% decrease in clean energy consumption rate compared to Scenario 3. This is because Scenario 2 did not consider the carbon trading mechanism, and the coupled system, from an economic perspective, will increase the output of coal-fired power generation units, increasing the system's carbon emissions. This indicates that the carbon certification collaborative mechanism can not only reduce carbon emissions but also increase the consumption rate of clean energy.

(3) CEEMDAN algorithm

To verify the effectiveness of the CEEMDAN algorithm in signal decomposition, it was compared with the EMD algorithm and the ensemble EMD (EEMD) algorithm using the mean absolute error (MAE), mean absolute percentage error (MAPE), and root mean square error (RMSE) as comparison metrics, as shown in Equation (30):
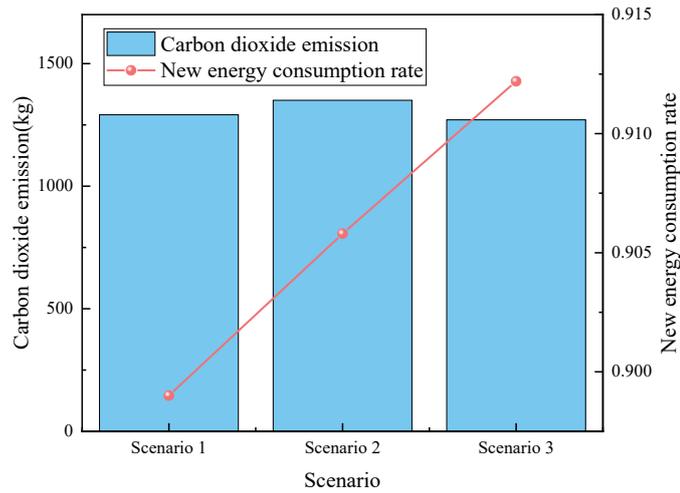
Fig. 10. Clean energy consumption rate and carbon dioxide emissions in three scenarios.

$$\begin{cases} R_{MSE} = \sqrt{\dfrac{\sum\limits_{t=1}^{24}\left(U_t^{\text{after}} - U_t^{\text{ac}}\right)^2}{24}} \\[4mm] M_{\text{APE}} = \dfrac{1}{24}\sum\limits_{t=1}^{24}\dfrac{\left|U_t^{\text{after}} - U_t^{\text{ac}}\right|}{U_t^{\text{ac}}} \\[4mm] M_{\text{AE}} = \dfrac{1}{24}\sum\limits_{t=1}^{24}\left|U_t^{\text{after}} - U_t^{\text{ac}}\right| \end{cases}$$

(30)

Where, U_t^{after} is the decomposed signal value at time t; U_t^{ac} is the actual signal value at time t.

Based on Equation (30), the comparative results are shown in Table 7.

As shown in Table 7, the EEMD algorithm reduces MAE, MAPE, and RMSE by 9.56%, 19.96%, and 7.13%, respectively, compared to the EMD algorithm. This is because EMD has a weaker ability to handle noise and mode mixing problems and is easily affected by signal noise. EEMD introduces random perturbations based on EMD and decomposes the original signal by adding different white noise multiple times to reduce random errors. The CEEMDAN algorithm reduces MAE, MAPE, and RMSE by 25.48%, 11.40%, and 35.76%, respectively, compared to the EEMD algorithm. This is because although EEMD solves some problems in EMD, there may still be modal aliasing issues. CEEMDAN can more effectively suppress false modes and improve the stability and accuracy of decomposition. This algorithm performed well in denoising and modal

decomposition tasks, effectively eliminating mode aliasing problems.

Applicability and Limitations Analysis

(1) Scenario expansion analysis

In order to expand the application scenarios of the model in this article, the CEEMDAN algorithm was used to solve it. The optimization scheduling model of the heat pump energy storage coupling system, considering the synergy and response characteristics of carbon certificates, was extended to typical days in different seasons throughout the year, where spring and autumn are collectively referred to as transition seasons. The scenario settings are shown in Table 8. The effectiveness analysis of the heat pump energy storage coupling system has fully verified that configuring energy storage devices can significantly reduce the system's external interaction costs. Therefore, energy storage devices are configured in all scenarios in the expansion analysis.

Based on the scenarios set in Table 8, Fig. 11 shows the total cost and clean energy consumption rate of typical days in the transition season, summer, and winter under different scenarios. The negative total cost represents the system's revenue.

Fig. 11 shows that in each season, the proposed optimization scheduling model for the heat pump energy storage coupling system considering carbon certification synergy and response characteristics (Scenario 6) has the lowest total cost and the highest clean energy consumption rate compared to other scenarios. The total cost of Scenario 6 during the transition season, summer, and winter, is -8524.37 yuan, -33671.25 yuan, and -25900.96 yuan, respectively. Compared to the other five scenarios, the average total cost is reduced by 0.93%, 0.89%, and 0.95%. From the perspective of clean energy consumption rate, Scenario 6 had clean energy consumption rates of 95.31%, 91.22%, and 89.39% in the transition season, summer, and winter,

Table 7. Comparison results of three types of algorithms.

	EMD	EEMD	CEEMDAN
MAE	118.65	107.31	79.97
MAPE	11.07%	8.86%	7.85%
RMSE	106.25	98.68	63.39

Table 8. Scenario settings for typical days in different seasons throughout the year.

Typical days of the year	Scenario	System composition		Cooperative mechanism	
		HP	TSE	CET	GCT
Typical days of the transition season	Scenario 1	×	√	√	×
	Scenario 2	√	√	√	×
	Scenario 3	×	√	×	√
	Scenario 4	√	√	×	√
	Scenario 5	×	√	√	√
	Scenario 6	√	√	√	√
Typical days of the summer season	Scenario 1	×	√	√	×
	Scenario 2	√	√	√	×
	Scenario 3	×	√	×	√
	Scenario 4	√	√	×	√
	Scenario 5	×	√	√	√
	Scenario 6	√	√	√	√
Typical days of the winter season	Scenario 1	×	√	√	×
	Scenario 2	√	√	√	×
	Scenario 3	×	√	×	√
	Scenario 4	√	√	×	√
	Scenario 5	×	√	√	√
	Scenario 6	√	√	√	√
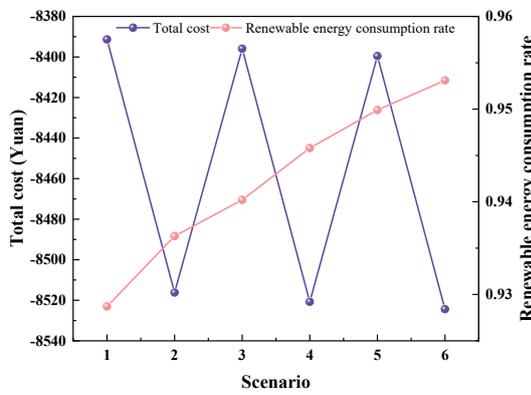
a) Typical days of the transition season
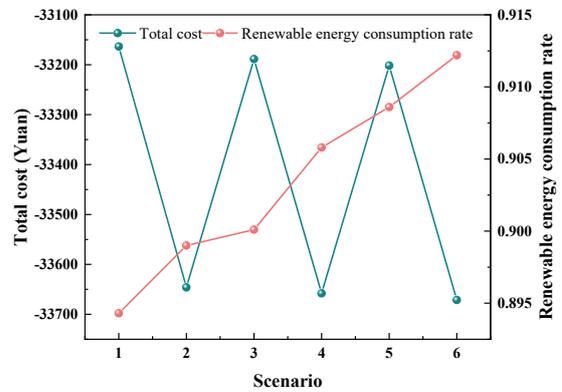
b) Typical days of the summer season
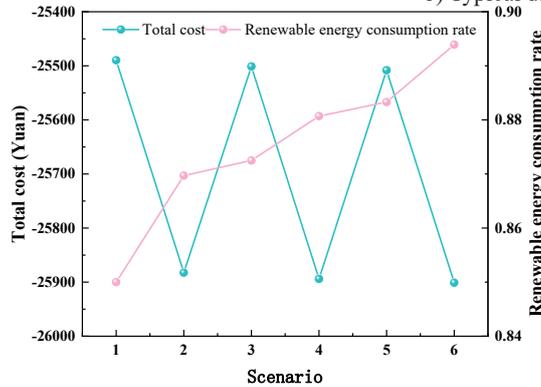
c) Typical days of the winter season

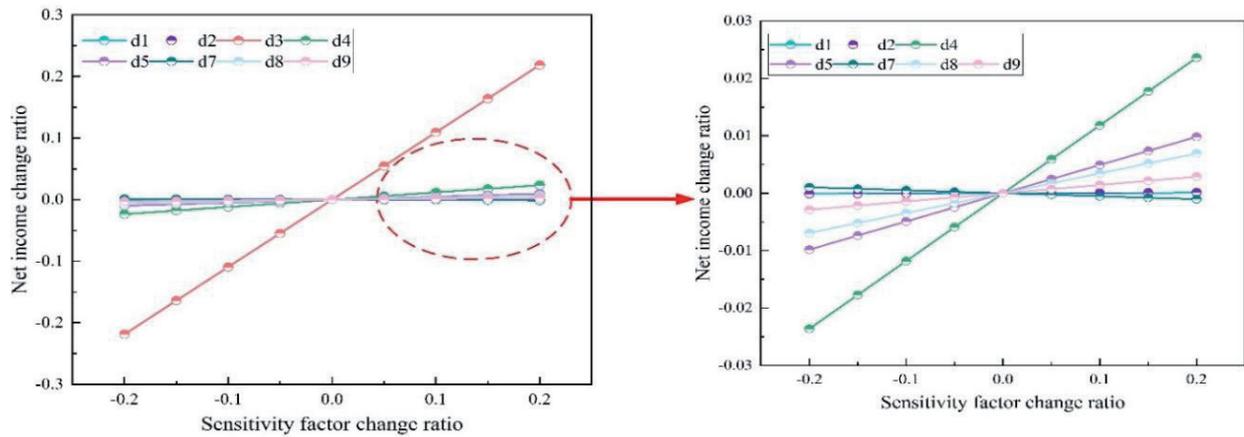Fig. 11. Total cost and clean energy consumption rate on different typical days throughout the year.

Fig. 12. Sensitivity analysis results.

respectively. Compared with the other five scenarios, the clean energy consumption rates increased by 1.36%, 1.17%, and 2.54%, respectively. This indicates that the model proposed in this article applies to typical daily scenarios throughout the year and can effectively improve the regional systems' revenue and clean energy consumption rate.

(2) Sensitivity analysis

In order to enhance the applicability of the model proposed in this article, sensitivity analysis was conducted by selecting the CO_2 trading benchmark price, unit green certificate price, internal unit electricity sales revenue, internal unit heat sales revenue, internal unit gas sales revenue, external unit electricity exchange price, external unit heat exchange price, and external gas exchange price as sensitivity factors. Record these sensitive factors as d1, d2, d3, d4, d5, d7, d8, and d9, respectively, and explore whether the variation range of sensitive factors within [-20%, 20%] affects the applicability of the model proposed in this paper, and analyze the limitations of the model proposed in this paper. The sensitivity analysis results are shown in Fig. 12.

As shown in Fig. 12, from the perspective of the impact of various factors on the system's net income, the changes in d1, d2, d3, d4, d5, d8, and d9 are all positively correlated with the net income of the system, while the external unit electricity exchange price (d7) is negatively correlated with the net income of the system. This is mainly because the interaction cost between the heat pump energy storage coupling system and the external power grid is positive. When the exchange price of external unit electricity increases, the interaction cost between the system and the external power grid also increases, resulting in a decrease in the system's net income of the system. From the perspective of the impact of various factors on the net income of the system, the internal unit sales revenue (d3) has the greatest impact on the net income of the system, with a sensitivity coefficient of 1.09, mainly because the internal sales revenue of the system accounts for the largest proportion. This indicates that in order to ensure

the stability of revenue, the heat pump energy storage coupling system needs to meet the electricity demand of internal users, and the system also needs to prevent and control the impact of unstable wind and photovoltaic power supply on the system in real time. If the system's power supply is unstable, it will cause a sharp decline in its net profit.

Conclusions

This paper takes the heat pump energy storage coupling system as the research object, considers carbon certification's synergy and response characteristics, and constructs a multi-objective optimization scheduling model for Western Australia with the highest clean energy consumption rate and total cost. A simulation analysis is carried out using a certain system as an example, and the simulation results show that:

(1) Compared to a single heat pump and energy storage system, a heat pump energy storage coupling system can reduce the system's energy purchase during peak hours and lower the system's operating costs and external interaction costs.

(2) Compared with the single CET and the GCT, the carbon certificate collaborative mechanism improves the driving force of the heat pump energy storage coupling system to absorb wind and photovoltaic power, reduces the output proportion of CFG units in the system, reduces carbon emissions, and increases the consumption rate of clean energy.

(3) Compared with EEMD and EMD algorithms, the CEEMDAN algorithm can more effectively suppress false modes, improve the stability and accuracy of decomposition, and demonstrate good performance in denoising and mode decomposition tasks.

Acknowledgments

Author Contributions

Study conception and design: Shenbo Yang, Yan Liang, Shaokang Qi; data collection: Shenbo Yang, Yan Liang; analysis and interpretation of results: Shenbo Yang, Yan Liang, Yuanying Chi; draft manuscript preparation: Junyao Shen, Ming Zhou. All authors reviewed the results and approved the final version of the manuscript.

Conflicts of Interest

The authors declare no conflict of interest.

References

1. IKEDA S., OOK R. Metaheuristic optimization methods for a comprehensive operating schedule of battery, thermal energy storage, and heat source in a building energy system. Applied Energy, **151**, 192, **2015**.
2. WALRAVEN D., LAENEN B., D'HAESELEER W. Economic system optimization of air-cooled organic Rankine cycles powered by low-temperature geothermal heat sources. Energy, **80**, 104, **2015**.
3. CAO S., SIREN K. Matching indices taking the dynamic hybrid electrical and thermal grids information into account for the decision-making of nZEB on-site renewable energy systems. Energy Conversion and Management, **101**, 423, **2015**.
4. HEDEGAARD K., BALYK O. Energy system investment model incorporating heat pumps with thermal storage in buildings and buffer tanks. Energy, **63**, 356, **2013**.
5. SMITH D.A., MAGO J.P., FUMO N. Emissions spark spread and primary energy spark spread – Environmental and energy screening parameters for combined heating and power systems. Applied Energy, **88** (11), 3891, **2011**.
6. ARAGAO A., GIAMPIETRO M. An integrated multi-scale approach to assess the performance of energy systems illustrated with data from the Brazilian oil and natural gas sector. Energy, **115**, 1412, **2016**.
7. LI W.W., QIAN T., ZHAO W., HUANG W.W., ZHANG Y., XIE X.H., TANG W.H. Decentralized optimization for integrated electricity–heat systems with data center based energy hub considering communication packet loss. Applied Energy, **350**,121586, **2023.**
8. NORD N., QVISTGAARD H.L., CAO G. Identifying key design parameters of the integrated energy system for a residential Zero Emission Building in Norway. Renewable Energy, **87**, 1076, **2016**.
9. HUGO A., ZMEUREANU R. Residential Solar-Based Seasonal Thermal Storage Systems in Cold Climates: Building Envelope and Thermal Storage. Energies, **5** (10), 3972, **2012**.
10. NOVO V.A., BAYON R.J., CASTRO F.D., HERNANDEZ J.R. Review of seasonal heat storage in large basins: Water tanks and gravel – water pits. Applied Energy, **87** (2), 390, **2009**.
11. XU Z., QI T.Y., OU X.M., ZHANG X.L. Research on the Energy and Economic Impacts of Multi-region Linked Emissions Trading System. Energy Procedia, **75** (C), 2495, **2015**.
12. LI F., WANG D., GUO H.D., ZHANG J.H. Distributionally Robust Optimization for integrated energy system accounting for refinement utilization of hydrogen and ladder-type carbon trading mechanism. Applied Energy, **367**, 123391, **2024**.
13. HUO S.S., LI Q., PU Y.C., XIE S.Q., CHEN W.R. Low carbon dispatch method for hydrogen-containing integrated energy system considering seasonal carbon trading and energy sharing mechanism. Energy, **308**, 132794, **2024**.
14. WANG T., GONG Y., JIANG C.W. A review on promoting share of renewable energy by green-trading mechanisms in power system. Renewable and Sustainable Energy Reviews, **40**, 923, **2014**.
15. WEI F., JING Z., WU Z.P., WU Q.H. A Stackelberg game approach for multiple energies trading in integrated energy systems. Applied Energy, **200**, 315, **2017**.
16. WANG L.L., XIA R.C., JIAO P.H., CHEN J.J., CHEN Y., LIU H.G. Multi-timescale optimization of integrated energy system with diversified utilization of hydrogen energy under the coupling of green certificate and carbon trading. Renewable Energy, **228**, 120597, **2024**.
17. XIANG Y., LIU Y.B., LIU J.Y., YANG W. A Chance-constrained Optimization Model for Determining Renewables Penetration Limit in Power Systems. Electric Power Components and Systems, **44** (7), 701, **2016**.
18. JIN S., LI Y., HUANG G., HAO Q., NIE S. Development of an integrated optimization method for analyzing effect of energy conversion efficiency under uncertainty – A case study of Bayingolin Mongol Autonomous Prefecture, China. Energy Conversion and Management, **106**, 687, **2015**.
19. JIN B.H., LIAO Y.C., LIU Z.C. Whether the off-design characteristics of equipment should be considered in integrated energy system optimization design models – A case study. Sustainable Cities and Society, **101**, 105146, **2024**.
20. RAUNER S., EICHHORN M., THRAN D. The spatial dimension of the power system: Investigating hot spots of Smart Renewable Power Provision. Applied Energy, **184**, 1038, **2016**.
21. PERNILLE S., ASGEIR T. Short-term uncertainty in long-term energy system models – A case study of wind power in Denmark. Energy Economics, **49**, 157, **2015**.
22. MAWIRE A., MAPHERSON. Experimental characterization of a thermal energy storage system using temperature and power controlled charging. Renewable Energy, **33** (4), 682, **2007**.
23. PASCUAL J., SANCHIS P, MARROYO L. Implementation and Control of a Residential Electrothermal Microgrid Based on Renewable Energies, a Hybrid Storage System and Demand Side Management. Energies, **7** (1), 210, **2014**.
24. STEFFEN B., WEBER C. Efficient storage capacity in power systems with thermal and renewable generation. Energy Economics, **36**, 556, **2013**.
25. CHENG C.P., XU Z. A Study on the Construction of China's Carbon EmissionsTrading System. Energy Procedia, **5** (C), 1037, **2011**.